

PAPER

One-way propagation of bulk states and robust edge states in photonic crystals with broken inversion and time-reversal symmetries

To cite this article: Jin-Cheng Lu *et al* 2018 *J. Opt.* **20** 075103

View the [article online](#) for updates and enhancements.

Related content

- [Topological phases in two-dimensional materials: a review](#)
Yafei Ren, Zhenhua Qiao and Qian Niu
- [Observation of topological edge states of acoustic metamaterials at subwavelength scale](#)
Hongqing Dai, Junrui Jiao, Baizhan Xia et al.
- [Topological valley-chiral edge states of Lamb waves in elastic thin plates](#)
Jian Wang and Jun Mei

One-way propagation of bulk states and robust edge states in photonic crystals with broken inversion and time-reversal symmetries

Jin-Cheng Lu[✉], Xiao-Dong Chen¹, Wei-Min Deng, Min Chen and Jian-Wen Dong[✉]

School of Physics & State Key Laboratory of Optoelectronic Materials and Technologies, Sun Yat-sen University, Guangzhou 510275, People's Republic of China

E-mail: stscm@mail.sysu.edu.cn and chenxd67@mail.sysu.edu.cn

Received 9 January 2018, revised 27 April 2018

Accepted for publication 10 May 2018

Published 1 June 2018



Abstract

The valley is a flexible degree of freedom for light manipulation in photonic systems. In this work, we introduce the valley concept in magnetic photonic crystals with broken inversion symmetry. One-way propagation of bulk states is demonstrated by exploiting the pseudo-gap where bulk states only exist at one single valley. In addition, the transition between Hall and valley-Hall nontrivial topological phases is also studied in terms of the competition between the broken inversion and time-reversal symmetries. At the photonic boundary between two topologically distinct photonic crystals, we illustrate the one-way propagation of edge states and demonstrate their robustness against defects.

Keywords: photonic crystals, one-way propagation, topological photonics

(Some figures may appear in colour only in the online journal)

1. Introduction

The valley degree of freedom (DoF) has been used to study valley-dependent Berry phase and valley-contrasting Hall transport in two-dimensional materials [1–5]. Regarding the similarity between electronic systems and classical systems, many fancy phenomena, e.g. valley vortex states and valley-spin locking behaviors, have been illustrated by expanding the concept of the valley DoF into sonic crystals [6–8], photonic crystals (PCs) [9–13] and plasmon crystals [14, 15]. Focusing on the inversion symmetry breaking bianisotropic PCs, the photonic valley-Hall effect has been demonstrated—that different spin flows in opposite valleys can be separately routed [10]. By inspecting the nontrivial topology, robust transport of valley-polarized edge states has been demonstrated when inter-valley scattering is prohibited [9, 11, 12]. On the other hand, nonreciprocal devices, e.g. photonic

waveguides and photonic isolators, are important in integrated photonic circuits. Magnetic media are among the time-reversal symmetry breaking materials that have been widely used in realizing nonreciprocal devices. For example, the analogue of the quantum Hall effect was theoretically proposed in gyoelectric or magnetic PCs [16–19], and then experimentally demonstrated in PCs by adapting magneto-optical materials [20, 21]. By employing the nonreciprocity and the nontrivial topology characterized by nonzero Berry phase, one-way propagation of electromagnetic (EM) waves has been realized [22–24]. Since then, magnetic PCs have been studied to observe topologically nontrivial edge states [25–28] and control wave propagation [29–32].

Generally, when one draws the band structure of honeycomb latticed structures, it is common to observe extrema points where maxima or minima of energy occur in momentum space. The term ‘valley’ is applied to these energy extrema [33]. Taking graphene with broken inversion symmetry as an example, there are two valleys of energy bands at the corners of

¹ Author to whom any correspondence should be addressed.

the Brillouin zone, viz. points K and K'. The intrinsic magnetic moment is concentrated in the valleys and has opposite signs at these two inequivalent valleys [1]. The Berry curvatures also have opposite values in these two valleys. It results in the opposite optical selection rules [2] and contrasting Hall transport with electrons flowing in opposite directions transverse to an in-plane electric field [3]. Because of the large separation between the two valleys in momentum space, scattering between them is strongly suppressed [34, 35], and hence the valley binary DoF is introduced to represent the local energy extrema at two corners of the Brillouin zone to distinguish their opposite physical quantities and distinct phenomena [4, 5, 33]. In this paper, we introduce the valley DoF in magnetic PCs and discuss the one-way propagation of bulk states and robust edge states. We first consider PCs with broken inversion and time-reversal symmetries, and present a model effective Dirac Hamiltonian (section 2). The broken symmetries of PCs lead to a pseudo-gap in which one-way propagation of bulk states is found (section 3). On altering the structural parameters of magnetic PCs, the competition of two broken symmetries gives rise to a topological phase transition (section 4). The valley-dependent edge states are found and their robustness against defects is also demonstrated (section 5). Lastly, we give a brief summary and discussion in section 6. The detailed derivation of the effective Hamiltonian is given in appendix A, and the simulation methods are shown in appendix B.

2. Photonic crystals with broken inversion and time-reversal symmetries

Let us start by considering a two-dimensional honeycomb PC with a lattice constant of $a = 15$ mm (figure 1(a)). The unit cell contains two circular rods embedded in an air background. Rod 1 has a diameter of $d_1 = 6$ mm, while rod 2 has a diameter of $d_2 = 5$ mm. As $d_1 \neq d_2$, the inversion symmetry is broken. In addition, the constitutive parameters of each rod

are set as $\varepsilon_r = 15.26$ and $\vec{\mu}_r = \begin{pmatrix} 0.78 & 0.93i & 0 \\ -0.93i & 0.78 & 0 \\ 0 & 0 & 1 \end{pmatrix}$. Note that

as the transverse magnetic modes are discussed in this work, the out-of-plane components of $\vec{\mu}_r$ (e.g. $\mu_{r,zz}$) have no influence on the band structure or the flow of light in the PC. These constitutive parameters correspond to those of a magnetic material at 6 GHz with an external magnetic field of 500 Oe and a saturation magnetization of 1884 Ga [36, 37]. With the introduction of an external magnetic field H_0 and the resulting nonzero non-diagonal permeability, the time-reversal symmetry is broken in this PC (called PC1 hereafter). Figure 1(b) shows the corresponding band structure of the transverse magnetic modes with nonzero z -component of electric fields. The band structure calculation and transmission results below are simulated using the commercial software COMSOL Multiphysics with the radio frequency module. As both inversion and time-reversal symmetries are broken, eigen-states at two inequivalent valleys, K and K', have different frequencies (compare band dispersions at K and K'). This is accurately predicted by considering the

effective Dirac Hamiltonian of honeycomb PCs with both inversion and time-reversal symmetries broken [9, 38]:

$$\hat{H} = f(\vec{q}) - f_0(\vec{K}) = \nu_D(\hat{\sigma}_x \hat{\tau}_z \delta k_x + \hat{\sigma}_y \delta k_y) + \lambda^P \hat{\sigma}_z + \lambda^T \hat{\sigma}_z \hat{\tau}_z, \quad (1)$$

where $f_0(\vec{K})$ is the degenerate Dirac frequency at points K and K' with inversion and time-reversal symmetries. $\delta \vec{k}$ is measured from point K or K'. $\hat{\sigma}_i$ and $\hat{\tau}_i$ are the Pauli matrices acting on sub-lattice and valley spaces, respectively (see detailed derivation of Hamiltonian in appendix A). Note that in equation (1), the perturbed frequencies with respect to $f_0(\vec{K})$ are considered. According to the Hamiltonian presented in equation (1), when bulk states at points K and K' are considered, we have $\delta k_x = \delta k_y = 0$. The two eigen-states at point K' ($\tau_z = -1$) have the frequencies of $f_1(K') = \lambda^P - \lambda^T$ for $\sigma_z = +1$ and $f_2(K') = -(\lambda^P - \lambda^T)$ for $\sigma_z = -1$. Similarly, the two eigen-states at point K ($\tau_z = +1$) have the frequencies of $f_1(K) = \lambda^P + \lambda^T$ for $\sigma_z = +1$ and $f_2(K) = -(\lambda^P + \lambda^T)$ for $\sigma_z = -1$. When the time-reversal symmetry is broken, i.e. $\lambda^T \neq 0$, then $\lambda^P - \lambda^T \neq \lambda^P + \lambda^T$ and $-(\lambda^P - \lambda^T) \neq -(\lambda^P + \lambda^T)$. This means that valley states at points K and K' have different frequencies, resulting in a pseudo-gap in which bulk states only exist in a single valley. For example, as indicated by the green rectangles in figure 1(b), there are two pseudo-gaps. The lower one ranges from 5.44 GHz to 5.78 GHz, the upper from 6.23 GHz to 6.82 GHz. Bulk states only exist in the K' valley in these two pseudo-gaps. Note that the band structure will be changed when the frequency-dependent permeability tensor is considered. For example, the frequency range of the second pseudo-gap will change to be from 6.13 GHz to 6.5 GHz with a smaller bandwidth due to the material dispersion. However, the one-way propagation of bulk states and edge states presented in the following sections are not substantially influenced by these effects. Note also that magnetic surface plasmon resonance has been found in dispersive magnetic media, leading to many interesting phenomena such as enhanced nonreciprocal scattering and beam steering [39–41]. As magnetic surface plasmon resonance is beyond the scope of this work, we carefully tune the structural parameters of our PC (e.g. the lattice constant) and focus on the frequency region near 6 GHz.

3. One-way propagation of bulk states

Employing the pseudo-gaps of PCs with broken inversion and time-reversal symmetries, a one-way propagation of bulk states is expected. To see this, we send a light beam with an incident angle of $\theta = 30^\circ$ from the upper-left (marked by the red arrow in figure 2(a)) into PC1 with the zigzag interface. The working frequency is taken to be inside the second pseudo-gap, viz. $f = 6.8$ GHz. When the incident wave encounters the photonic interface, it will be refracted into PC1. The direction of the refracted beam can be determined from the isofrequency diagram which is shown in figure 2(b). Due to the frequency asymmetry induced by broken inversion and time-reversal symmetries, the isofrequency diagram

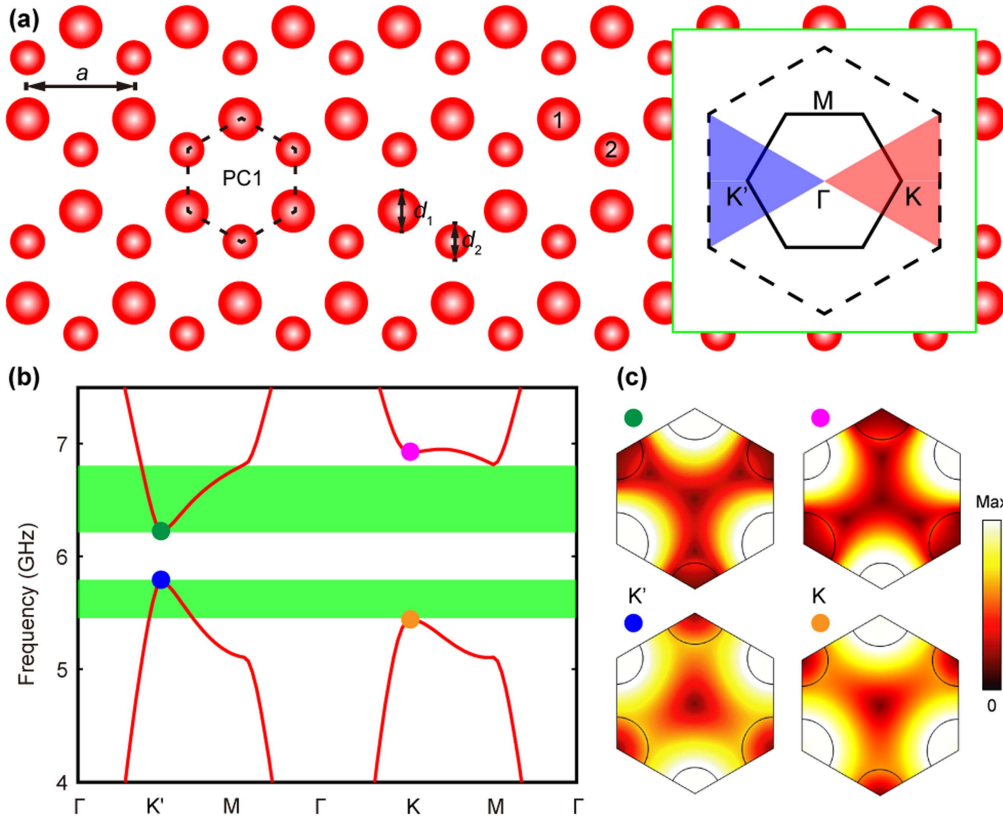


Figure 1. (a) A honeycomb magnetic photonic crystal with lattice constant $a = 15$ mm. The unit cell is outlined by the dashed hexagon in which the diameters of rod 1 and rod 2 are 6 mm and 5 mm respectively. The boundaries of the first Brillouin zone and the third Brillouin zone are respectively outlined by solid and dashed black lines in the right inset. (b) The band structure of the transverse magnetic modes with nonzero z -component of electric fields (E_z). Two pseudo-gaps, in which bulk states only exist in a single valley, are shaded in green. (c) The amplitude of E_z of four eigen-states at points K and K'.

ranging from 6.23 to 6.8 GHz only exists in the K' valley. For the chosen frequency of $f = 6.8$ GHz, i.e. $fa/c = 0.34$, we superimpose the contour of the incident medium (air, a dashed black circle with $f = c|\mathbf{k}|/2\pi$). The incident wave corresponds to the red arrow. According to the Bloch theorem under Bragg scattering, only states with the same $k_{||}$ can be excited. To select states with the same $k_{||}$, we draw a dashed black line through the incident wave vector (\mathbf{k}) and perpendicular to the interface (here, along the ΓM direction). This dashed line intersects with the isofrequency contours at two places, but only the upper one determines the refracted beam direction as its group velocity points toward the crystal from the interface (green arrow). As the incident and refracted beams lie at the same side of the normal of interface, negative refraction will occur. This is well confirmed by the incident and refracted beams in the upper interface in figure 2(a). When the refracted wave beam encounters the lower interface, the negative refraction happens again. The output wave beam lastly propagates into air with a positive angle of 30° (marked by the blue arrow in figures 2(a) and (b)). However, as both inversion and time-reversal symmetries are broken, such a wave beam cannot go back through the same path. To see this, we consider incident transmission in which the light beam arrives from the lower-right corner with an incident angle of 30° (figure 2(c)). Once again, we draw a dashed

black line through the incident \mathbf{k} and perpendicular to the interface (figure 2(d)). This dashed line has no intersection with the isofrequency contour of PC1, and hence the incident wave will be totally reflected. The simulation result is in good agreement with the theoretical prediction (figure 2(c)). By the comparison between transmissions in figures 2(a) and (c), one-way propagation of bulk states is demonstrated. Note that in order to have one-way propagation of bulk states, the bandwidth of the pseudo-gap should be larger than 3.2%, which corresponds to a PC with $d_1 > 5.65$ mm and $d_2 < 5.35$ mm. The PC in figure 1 has a pseudo-gap with a bandwidth of 9.0%, which is large enough to observe the one-way propagation of bulk states, as shown in figure 2.

4. Topological phase transition

Besides the one-way propagation of bulk states, nontrivial topology related to gapping out Dirac cones at the corner of the Brillouin zone can be also found in PC1. The topology of a PC is related to the Berry curvature of the lowest band, which is defined as $\Omega(\vec{k}) \equiv i\nabla_{\vec{k}} \times [\langle u_{\vec{k}} | \nabla_{\vec{k}} | u_{\vec{k}} \rangle]$, where $u_{\vec{k}}$ is the electromagnetic field and $\langle \dots \rangle$ is integrated within the unit cell. By integrating the Berry curvature near the K (K') valley which is marked in red (blue) in the right inset of figure 1(a),

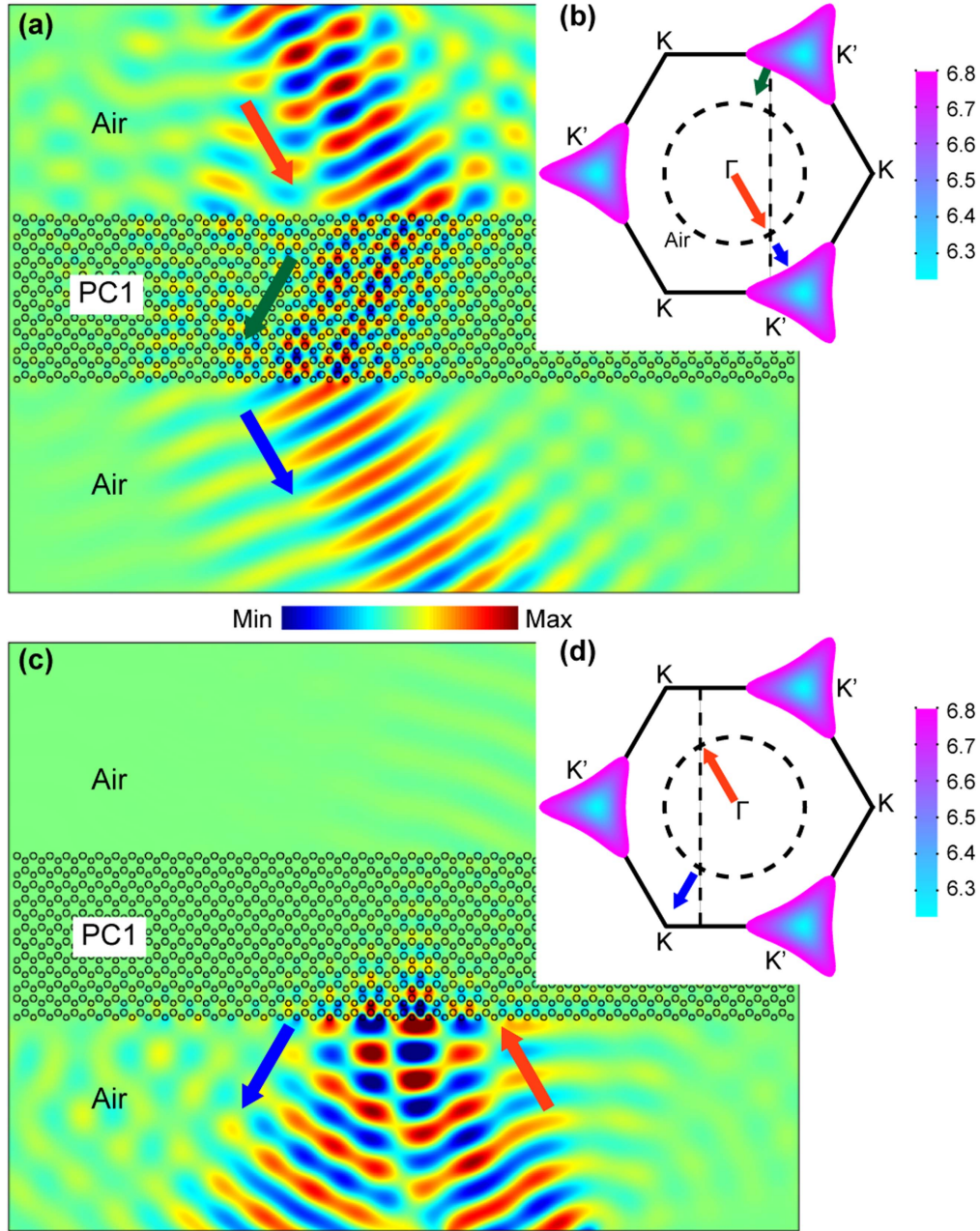


Figure 2. One-way propagation of bulk states and the isofrequency diagram. (a) Simulation for incident light beam with an oblique angle of 30° from upper left (indicated by a red arrow) at the frequency of 6.8 GHz. The negative refraction happens at the photonic interfaces between the PC and the air background. (b) Isofrequency diagram of PC1 for frequencies ranging from 6.23 GHz to 6.8 GHz. The dashed circular lines mark the contour of the incident and output medium, i.e. air. The red, green, and blue arrows indicate the propagation directions of EM flow in the upper air, PC, and lower air regions, respectively. (c) Simulation for incident light beam with an oblique angle of 30° from lower right (indicated by a red arrow) at the frequency of 6.8 GHz. The incident wave is totally reflected. (d) Isofrequency diagram and EM flow directions for figure 2(c).

one can obtain the Chern number, C_K ($C_{K'}$), which characterizes the topological phase. Based on the Hamiltonian presented in equation (1), the Chern number is given by $C_{\tau_z} = \tau_z \cdot \text{sgn}(\lambda^P + \lambda^T \tau_z) / 2$ [1, 9, 38]. Here, the valley index τ_z takes the value of $+1$ (-1) for the K (K') valley. We take PC1 in figure 1 as an example to show the concrete calculation of C_K and $C_{K'}$. The amplitude of E_z fields of four eigen-states at points K and K' are shown in figure 1(c). At point K , the electric field of the bulk state with the lower frequency is mostly

located at rod 1, which corresponds to the $\sigma_z = +1$ state. That is to say, $f_1(K) < f_2(K) \Rightarrow \lambda^P + \lambda^T < -(\lambda^P + \lambda^T) \Rightarrow \lambda^P + \lambda^T < 0$. So we have $C_K = 1 \cdot \text{sgn}(\lambda^P + \lambda^T) / 2 = 1 \cdot (-1) / 2 = -1/2$. In contrast, at point K' , the bulk state with the lower frequency has its electric field mostly located at rod 2, which corresponds to the $\sigma_z = -1$ state. Then $f_2(K') < f_1(K') \Rightarrow -(\lambda^P - \lambda^T) < \lambda^P - \lambda^T \Rightarrow \lambda^P - \lambda^T > 0$, so we have $C_{K'} = -1 \cdot \text{sgn}(\lambda^P - \lambda^T) / 2 = -1 \cdot (1) / 2 = -1/2$. Hence, it belongs to the quantum Hall phase with nonzero Chern

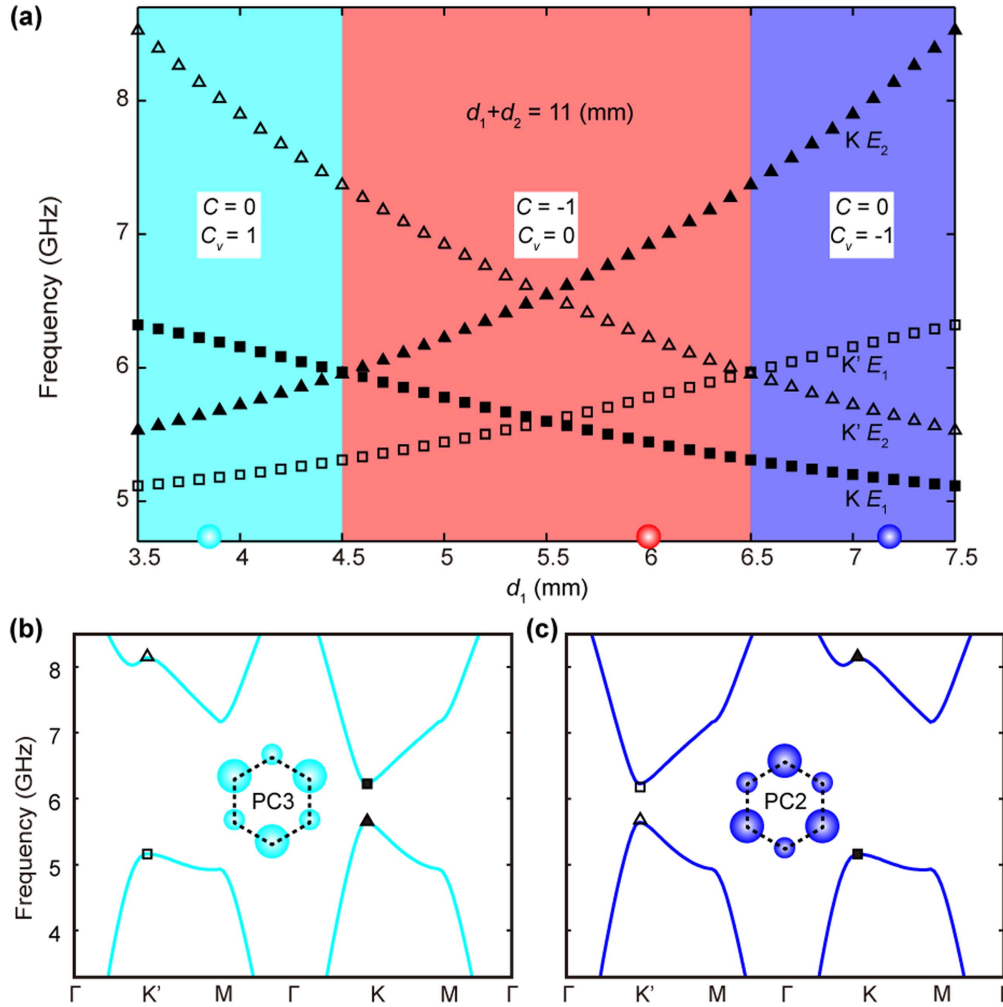


Figure 3. Frequency spectra of four states at points K and K', and band structures of two more PCs. (a) Mode evolution of four eigen-states at points K and K' as a function of the diameter of rod 1, i.e. d_1 . Modes with electric fields concentrated at rod 1 and rod 2 are respectively marked by triangles and squares. Solid and hollow markers represent modes of points K and K' respectively. Under the competition between broken time-reversal and inversion symmetries, a topological phase transition occurs when mode exchange happens at point K or K'. Three topologically distinct phases with different Chern and valley Chern numbers are shaded in different colors. (b) Band structure for PC3, with $d_1 = 3.8$ mm and $d_2 = 7.2$ mm. (c) Band structure for PC2, with $d_1 = 7.2$ mm and $d_2 = 3.8$ mm.

number $C = C_K + C_{K'} = -1$ and zero valley Chern number $C_v = C_K - C_{K'} = 0$. The Chern number and valley Chern number are two invariants which characterize the topological properties of band structures of PCs. They determine the number and group velocity of edge states when a photonic boundary is considered. Considering PC1, its nontrivial topological phase is dominated by the broken time-reversal symmetry. A topological transition is expected to result from the competition between two broken symmetries. To see this, we alter the diameters of the two rods d_1 and d_2 , to change the strength of the broken inversion symmetry. In contrast, we keep $(d_1 + d_2)$ unchanged to approximately maintain the strength of broken time-reversal symmetry. Figure 3(a) shows the frequency spectra of four states at points K and K' as a function of d_1 . As we can see, three topological phases with different topological invariants are found. The abovementioned PC1 in figure 1(b) is characterized by $C = -1$ and $C_v = 0$. This topological phase is shaded in red in figure 3(a). With the increase of d_1 and the simultaneous decrease of d_2 , the two states at point K point move apart. In

contrast, the two states at K' point come close, meet each other (at $d_1 = 6.48$ mm), and separate. With this mode exchange, the band gap is closed and reopened. After such a topological phase transition, the effect of broken inversion symmetry is dominant, and the resulting magnetic PC is characterized by $C = 0$ and $C_v = -1$ (i.e. the valley-Hall phase). Figure 3(c) shows the band structure of one representative PC with $d_1 = 7.2$ mm and $d_2 = 3.8$ mm (the unit cell is shown in the inset; we refer to this PC as PC2 hereafter). Band asymmetry for eigen-states in the K and K' valleys is also found. When we decrease d_1 while increasing d_2 , the behavior of states at points K and K' evolves differently. There exists a mode exchange for states at point K when $d_1 = 4.52$ mm, but no mode exchange happens for states at point K'. With the mode exchange at point K, the PC topology is characterized by $C = 0$ and $C_v = 1$ (i.e. another valley-Hall phase). A representative PC with $d_1 = 3.8$ mm and $d_2 = 7.2$ mm (called PC3 hereafter) and its band structure are shown in figure 3(b).

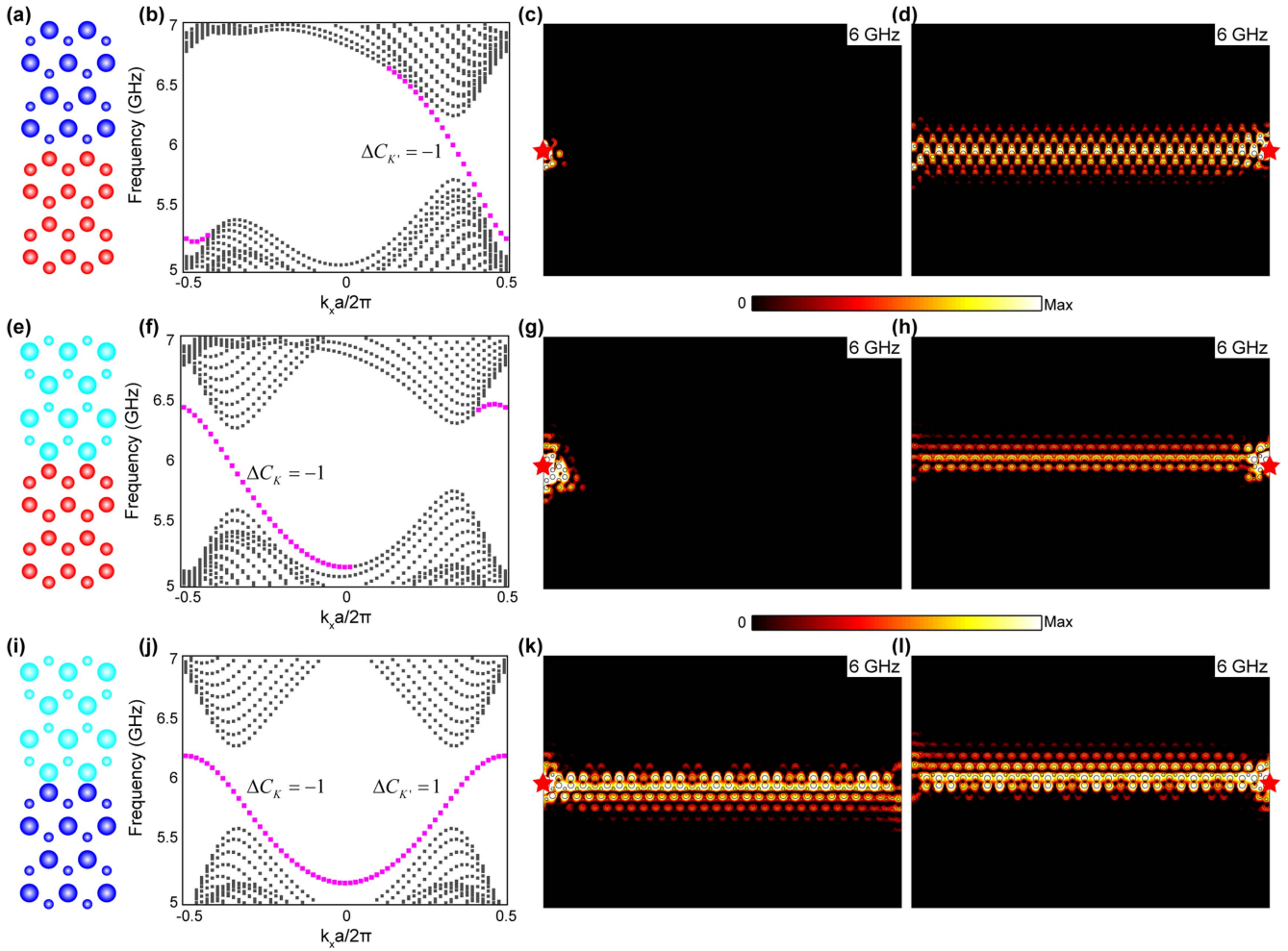


Figure 4. One-way propagation of edge states. (a) Schematic of photonic boundary constructed by PC1 (red) at the bottom and PC2 (blue) at the top. (b) Projected band structure in which bulk states are shaded in black and edge states in pink. There exists one gapless edge state with negative group velocity at the K' valley. (c), (d) The transmission of edge states at 6 GHz when the excited source is put at the (c) left end and (d) right end. One-way propagation of edge states is demonstrated on comparing figures 4(c) and 4(d). (e)–(h) Schematic of photonic boundary constructed by PC1 at the bottom and PC3 at the top, the projected band structure, and one-way propagation of edge states. (i) The schematic of photonic boundary which is constructed by PC2 (blue) at the bottom and PC3 (cyan) at the top. (j) Projected band structure: bulk states are shaded in black, edge states in pink. Valley-dependent edge states are found at two inequivalent valleys. (k), (l) Transmission of edge states at 6 GHz when the excited source is put at the (k) left end and (l) right end. Both leftward and rightward EM flows are excited.

5. One-way propagation of edge states and their robustness

With these three topological phases, protected edge states at the photonic boundary between topologically distinct PCs will be found. Figure 4 shows three different photonic boundaries. In figure 4(a), we build up a photonic boundary with PC1 at the bottom and PC2 at the top. For PC1, we have $C_K = -1/2$ and $C_{K'} = -1/2$, while for PC2, $C_K = -1/2$ and $C_{K'} = 1/2$. The Chern number difference across the boundary is then 0 at valley K while it is -1 at K' . As a result, there is one gapless edge state with negative group velocity across the K' valley (figure 4(b)). One-way propagation of these edge states is expected as their counter-propagating states are missing. For example, at the frequency of 6 GHz, leftward EM waves can be excited when the input source is placed on the right (figure 4(d)). However, no EM flow can be observed when the source is put on the left (figure 4(c)). Comparison between figures 4(c) and (d)

demonstrates the one-way propagation of edge states. By replacing PC2 in the first photonic boundary with PC3, we obtain the second photonic boundary, with PC1 on the bottom and PC3 on the top (figure 4(e)). For this boundary, the Chern number difference across valley K is -1 , and gapless edge states with negative group velocity are found near K (figure 4(f)). However, no edge states can be found near valley K' . Similarly, one-way propagation of edge state is also demonstrated (figures 4(g) and (h)). Note that by inference from the excited field distribution in figures 4(d) and (h), these two edge states are different, although both of them propagate leftwards. Lastly, we consider the photonic boundary consisting of two PCs with different valley Chern number (figure 4(i) with PC3 on the top and PC2 on the bottom). According to the Chern number difference, edge states with negative group velocity exist at valley K; those with positive group velocity, at valley K' (figure 4(j)). As a result, both sources on the left or right can excite EM waves along the boundary (figures 4(k) and (l)).

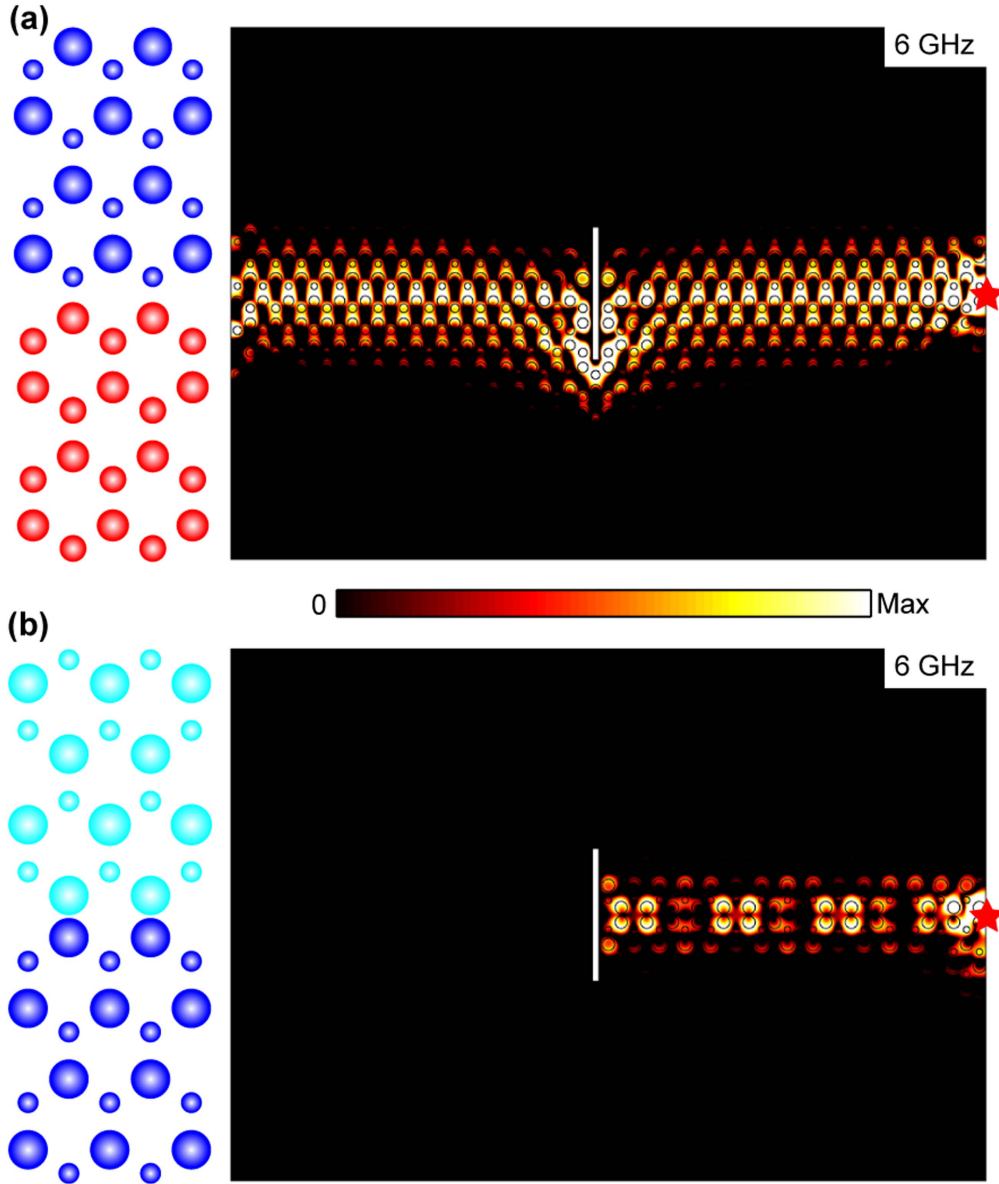


Figure 5. Robustness of edge states. (a) A metallic obstacle is inserted into the center of the photonic waveguide constructed by PC1 at the bottom and PC2 at the top. When the incident source (red star) is put at the right end, the excited leftward EM flow can go around the metallic obstacle, and no backscattering is observed. (b) The transmission of edge state at the photonic boundary between PC2 and PC3 when a metallic obstacle is inserted in the boundary. As the inter-valley scattering is not suppressed, strong backscattering is observed, and no transmission is obtained at the left end.

Gapless edge states are robust against defects and disorders. For example, we insert a metallic plate as an insulating obstacle in the middle of the first photonic waveguide, and put the incident source at the right side (figure 5(a)). The excited leftward EM flow can go around the metallic obstacle and keep moving leftwards. No backscattering is observed, and perfect transmission is demonstrated. In contrast, although the valley-dependent edge states shown in figure 4(i) are robust against some sharp corners [11], they suffer backscattering when inter-valley scattering is not suppressed. As presented in figure 5(b), excited leftward edge states at the photonic boundary between PC2 and PC3 are strongly reflected when the same metallic obstacle is inserted vertically into the boundary. No transmission can be detected at the left end.

6. Conclusion

To conclude, we have extended valley DoF into magnetic PCs with broken inversion symmetry. Under both broken time-reversal and inversion symmetries, two pseudo-gaps where the bulk states only exit at one single valley are obtained. This results in the one-way propagation of bulk states in a single PC. Further, we have also demonstrated the topological phase transition induced by the competition between two broken symmetries. By constructing photonic boundaries between PCs within different topological phases, one-way edge states which are robust against certain defects are illustrated. Our work provides a potential way to realize one-way devices such as waveguides and filters in the

microwave range where magnetic materials with large time-reversal symmetry breaking response can be found. Although magnetic materials are rare and usually have limited time-reversal breaking response in the optical regime, on-chip optical isolation [42] and nonreciprocal lasing [43] have recently been realized in near-infrared frequencies. This provides inspiration to extend the valley-related properties presented in this work into the optical regime.

Acknowledgments

This work is supported by Natural Science Foundation of China (11522437, 61775243, 11704422), Guangdong Natural Science Funds for Distinguished Young Scholar (S2013050015694) and Fundamental Research Funds for the Central Universities (No. 17lgpy19).

Appendix A. Photonic effective Hamiltonian

In this appendix, we derive the effective Hamiltonian of magnetic PCs with broken inversion and time-reversal symmetries. As the transverse magnetic modes with nonzero (H_x, H_y, E_z) are considered, the related constitutive parameters are the out-of-plane relative permittivity ε_z and the in-plane relative permeability $\tilde{\mu}_{||} = \begin{pmatrix} \mu_{xx} & i\mu_{xy} \\ -i\mu_{xy} & \mu_{xx} \end{pmatrix}$. The corresponding Maxwell equations are:

$$\begin{aligned} \partial_y E_z &= i\omega\mu_0(\mu_{xx}H_x + i\mu_{xy}H_y) \\ -\partial_x E_z &= i\omega\mu_0(\mu_{xx}H_y - i\mu_{xy}H_x) \\ \partial_x H_y - \partial_y H_x &= -i\omega\varepsilon_0\varepsilon_z E_z. \end{aligned} \quad (\text{A1})$$

By expressing H_x and H_y in terms of E_z , we get:

$$\omega^2\mu_0\varepsilon_0\varepsilon_z E_z + (\partial_x m \partial_x + \partial_y m \partial_y) E_z = i(\partial_x \theta \partial_y - \partial_y \theta \partial_x) E_z, \quad (\text{A2})$$

where $m = \mu_{xx}/(\mu_{xx}^2 - \mu_{xy}^2)$, and $\theta = \mu_{xy}/(\mu_{xx}^2 - \mu_{xy}^2)$. Utilizing the periodicity of the photonic crystals, we expand the fields and the constitutive parameters as $E_z(\vec{r}, \vec{q}) = \sum_{\vec{G}} E_{\vec{G}} e^{i(\vec{q} + \vec{G}) \cdot \vec{r}}$, $\varepsilon_z(\vec{r}) = \sum_{\vec{G}} \beta_{\vec{G}} e^{i\vec{G} \cdot \vec{r}}$, $m(\vec{r}) = \sum_{\vec{G}} m_{\vec{G}} e^{i\vec{G} \cdot \vec{r}}$, and $\theta(\vec{r}) = \sum_{\vec{G}} \theta_{\vec{G}} e^{i\vec{G} \cdot \vec{r}}$. By substituting these into equation (A2), the linear equations for the Fourier components of E_z can be obtained:

$$\begin{aligned} \omega^2\mu_0\varepsilon_0 \sum_{\vec{G}'} \beta_{\vec{G}-\vec{G}'} E_{\vec{G}'} - \sum_{\vec{G}'} e_{\vec{G}-\vec{G}'} \{ (q_x + G_x)(q_x + G'_x) \\ + (q_y + G_y)(q_y + G'_y) \} E_{\vec{G}'} &= -i \sum_{\vec{G}'} \theta_{\vec{G}-\vec{G}'} \{ (q_x + G_x) \\ \times (q_y + G'_y) + (q_y + G_y)(q_x + G'_x) \} E_{\vec{G}'}. \end{aligned} \quad (\text{A3})$$

Next, we focus on two time-reversal but inequivalent valleys: K and K'. First, for the K valley, we truncate the plane wave basis to the first three plane waves near point Γ . The basis for these plane waves basis comprises the three equal-length reciprocal vectors: $\vec{K} + \vec{G}_i$ each rotating $2\pi/3$

with respect to one another, where $\vec{K} = [K, 0]$ ($K = 4\pi/3a$) and $\vec{G}_0 = [0, 0]$, $\vec{G}_1 = [-3K/2, -\sqrt{3}K/2]$, $\vec{G}_2 = [-3K/2, \sqrt{3}K/2]$. In addition, we have $q_x = K + \delta k_x$ and $q_y = \delta k_y$ in the vicinity of point K. Then a 3×3 equation can be obtained for the Fourier components of field E_z :

$$(\hat{m} + \hat{\theta})\tilde{E} = \omega^2\mu_0\varepsilon_0\hat{\beta}\tilde{E} \quad (\text{A4})$$

$$\begin{aligned} \text{with } \hat{m} &= K^2 \begin{pmatrix} m_{G_0} & -\frac{1}{2}m_{G_1} & -\frac{1}{2}m_{G_1} \\ -\frac{1}{2}m_{G_1} & m_{G_0} & -\frac{1}{2}m_{G_1} \\ -\frac{1}{2}m_{G_1} & -\frac{1}{2}m_{G_1} & m_{G_0} \end{pmatrix} + K\delta k_x \\ &\times \begin{pmatrix} 2m_{G_0} & \frac{1}{2}m_{G_1} & \frac{1}{2}m_{G_1} \\ \frac{1}{2}m_{G_1} & -m_{G_0} & -m_{G_1} \\ \frac{1}{2}m_{G_1} & m_{G_1} & -m_{G_0} \end{pmatrix} \\ &+ K\delta k_y \times \begin{pmatrix} 0 & -\frac{\sqrt{3}}{2}m_{G_1} & \frac{\sqrt{3}}{2}m_{G_1} \\ -\frac{\sqrt{3}}{2}m_{G_1} & -\sqrt{3}m_{G_0} & 0 \\ \frac{\sqrt{3}}{2}m_{G_1} & 0 & \sqrt{3}m_{G_0} \end{pmatrix}, \\ \hat{\theta} &= \frac{-\sqrt{3}i}{2}K^2\theta_{G_1} \begin{pmatrix} 0 & -1 & 1 \\ 1 & 0 & -1 \\ -1 & 1 & 0 \end{pmatrix}, \quad \hat{\beta} = \begin{pmatrix} \beta_{G_0} & \beta_{G_2} & \beta_{G_1} \\ \beta_{G_1} & \beta_{G_0} & \beta_{G_2} \\ \beta_{G_2} & \beta_{G_1} & \beta_{G_0} \end{pmatrix} \text{ and} \\ \tilde{E} &= [E_{G_0}; E_{G_1}; E_{G_2}]. \text{ Note that here we neglect the high} \\ &\text{order perturbation induced by the inversion asymmetric} \\ &\text{component of } m(\vec{r}) \text{ and } \theta(\vec{r}). \text{ Using the transformation} \\ &[\hat{U}, \hat{0}; \hat{0}, \hat{U}], \text{ where } \hat{U} = [1, 1, 1; 1, \eta^2, \eta; 1, \eta, \eta^2]/\sqrt{3} \text{ and} \\ &\eta = \exp(i2\pi/3), \text{ one can obtain the Dirac bands by elim-} \\ &\text{inating the monopolar band:} \\ &\left[K^2 \left(m_{G_0} + \frac{1}{2}m_{G_1} \right) + K(m_{G_0} - m_{G_1})(\hat{\sigma}_x \delta k_x + \hat{\sigma}_y \delta k_y) \right. \\ &\left. - \frac{3}{2}K^2\theta_{G_1}\hat{\sigma}_z \right] E_d = \omega(\vec{q})^2\mu_0\varepsilon_0 \left[\left(\beta_{G_0} - \frac{1}{2}\beta_{G_1} - \frac{1}{2}\beta_{G_2} \right) \right. \\ &\left. + \frac{i\sqrt{3}}{2}(\beta_{G_2} - \beta_{G_1}) \right] E_d, \end{aligned} \quad (\text{A5})$$

where $E_d = [E_{G_1}; E_{G_2}]$ and $\hat{\sigma}_i$ are Pauli matrices acting on the sub-lattices. When $\vec{q} = \vec{K}$ is studied, and first considering the inversion symmetric case with time-reversal symmetry, we have the Dirac frequency: $f_0(\vec{K}) = \frac{K(m_{G_0} + m_{G_1}/2)}{c[\mu_0\varepsilon_0(\beta_{G_0} - \beta_{G_1}/2 - \beta_{G_2}/2)]^{1/2}}$, where c is the speed of light in vacuum. After introducing the broken inversion symmetry by the asymmetric $\varepsilon_z(\vec{r})$ and broken time-reversal symmetry by the nonzero $\theta(\vec{r}) = \mu_{xy}/(\mu_{xx}^2 - \mu_{xy}^2)$,

equation (A5) is reduced to

$$[\nu_D(\hat{\sigma}_x \delta k_x + \hat{\sigma}_y \delta k_y) + \lambda^P \hat{\sigma}_z + \lambda^T \hat{\sigma}_z] E_d = \Delta f(\vec{q}) E_d, \quad (\text{A6})$$

where

$$\nu_D = \frac{\omega_0(\vec{K})(m_{G_0} - m_{G_1})}{2cK(m_{G_0} + m_{G_1}/2)},$$

$$\lambda^P = \frac{i\sqrt{3}\mu_0\varepsilon_0\omega_0^3(\vec{K})(\beta_{G_1} - \beta_{G_2})}{4cK^2(m_{G_1} + m_{G_2}/2)},$$

$$\lambda^T = -\frac{\sqrt{3}\theta_{G_1}}{4cK(m_{G_1} + m_{G_2}/2)}, \quad \Delta f(\vec{q}) = f(\vec{q}) - f_0(\vec{K}).$$

The above procedure can be repeated around the K' valley ($\vec{K}' = [-K, 0]$), and we get

$$[\nu_D(-\hat{\sigma}_x \delta k_x + \hat{\sigma}_y \delta k_y) + \lambda^P \hat{\sigma}_z - \lambda^T \hat{\sigma}_z] E_d = \Delta f(\vec{q}) E_d. \quad (\text{A7})$$

By introducing valley Pauli matrices $\hat{\tau}_i$ ($\tau_z = +1$ for point K and $\tau_z = -1$ for K'), we obtain the photonic effective Hamiltonian, as shown in equation (1) of the main text:

$$\hat{H} = f(\vec{q}) - f_0(\vec{K}) = \nu_D(\hat{\sigma}_x \hat{\tau}_z \delta k_x + \hat{\sigma}_y \delta k_y) + \lambda^P \hat{\sigma}_z + \lambda^T \hat{\sigma}_z \hat{\tau}_z. \quad (\text{A8})$$

Appendix B. Simulation methods

The simulations in the main text were performed with COMSOL Multiphysics. The unit cell of the honeycomb PC is shown in figure B1(a). Two rods (shaded in blue) are set as magnetic medium, and the background is set as air. Three pairs of boundaries (i.e. boundaries of 1 and 4, 2 and 5, 3 and 6) are set as the periodic condition with the Floquet periodicity (figure B1(b)). We sweep the wave vector along the first Brillouin zone boundary (i.e. $\Gamma K' M \Gamma K M \Gamma$) to calculate the bulk band structure (figure B1(c)).

The simulated structure of one-way propagation of bulk states in figure 2 is shown in figure B2(a) in which the magnetic PCs are marked in blue. One section of the upper boundary (marked in red) is set as scattering boundary condition with a nonzero amplitude as the incident source (figure B2(b)). The remaining outmost boundaries (marked in blue) are set as scattering boundary with zero amplitude to guide electromagnetic waves.

The edge state band dispersions shown in figure 4 were obtained using a supercell with height of $20\sqrt{3}a$. The scattering boundary condition was applied along the y-direction and the periodic boundary condition was applied along the x-direction.

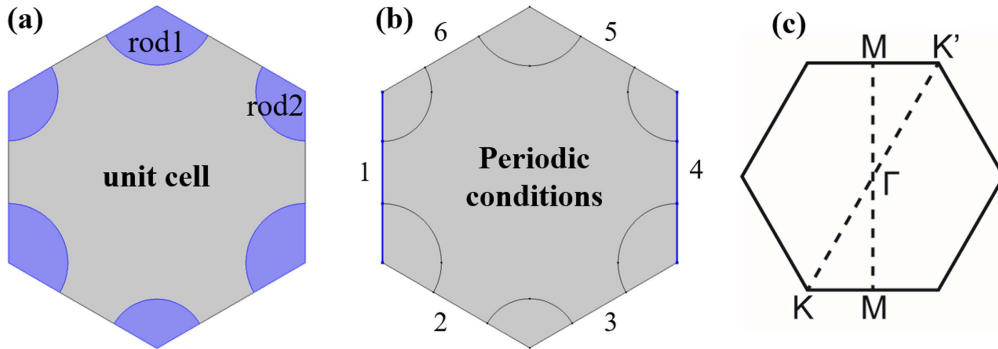


Figure B1. (a) Schematic of the unit cell of the honeycomb PC. (b) The settings of three pairs of periodic boundaries. (c) Schematic of the first Brillouin zone.

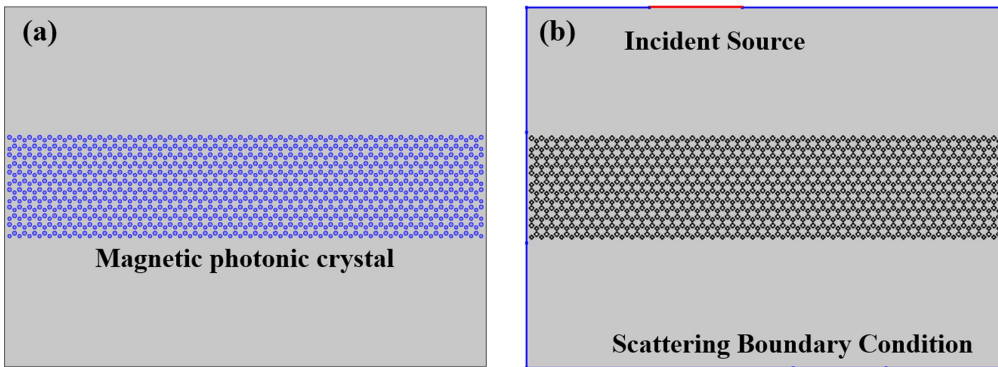



Figure B2. (a) Schematic of the simulated structure for one-way propagation of bulk states presented in figure 2. Here the magnetic PC is marked in blue. (b) The scattering boundary condition is applied on the outmost boundary in which the source is marked in red.

ORCID iDs

Jin-Cheng Lu  <https://orcid.org/0000-0001-7526-3655>Jian-Wen Dong  <https://orcid.org/0000-0003-2379-554X>

References

- [1] Xiao D, Yao W and Niu Q 2007 Valley-contrasting physics in graphene: magnetic moment and topological transport *Phys. Rev. Lett.* **99** 236809
- [2] Mak K F, McGill K L, Park J and McEuen P L 2014 The valley Hall effect in MoS₂ transistors *Science* **344** 1489–92
- [3] Ye Y, Wong Z J, Lu X, Ni X, Zhu H, Chen X, Wang Y and Zhang X 2015 Monolayer excitonic laser *Nat. Photon.* **9** 733–7
- [4] Lensky Y D, Song J C, Samutpraphoot P and Levitov L S 2015 Topological valley currents in gapped Dirac materials *Phys. Rev. Lett.* **114** 256601
- [5] Yao W, Xiao D and Niu Q 2008 Valley-dependent optoelectronics from inversion symmetry breaking *Phys. Rev. B* **77** 235406
- [6] Lu J, Qiu C, Ke M and Liu Z 2016 Valley vortex states in sonic crystals *Phys. Rev. Lett.* **116** 093901
- [7] Lu J, Qiu C, Ye L, Fan X, Ke M, Zhang F and Liu Z 2016 Observation of topological valley transport of sound in sonic crystals *Nat. Phys.* **13** 369–74
- [8] Huo S Y, Chen J J, Huang H B and Huang G L 2017 Simultaneous multi-band valley-protected topological edge states of shear vertical wave in two-dimensional phononic crystals with veins *Sci. Rep.* **7** 10335
- [9] Ma T and Shvets G 2016 All-Si valley-Hall photonic topological insulator *New J. Phys.* **18** 025012
- [10] Dong J W, Chen X D, Zhu H, Wang Y and Zhang X 2017 Valley photonic crystals for control of spin and topology *Nat. Mater.* **16** 298–302
- [11] Chen X D, Zhao F L, Chen M and Dong J W 2017 Valley-contrasting physics in all-dielectric photonic crystals: orbital angular momentum and topological propagation *Phys. Rev. B* **96** 020202(R)
- [12] Noh J, Huang S, Chen K and Rechtsman M C 2018 Observation of photonic topological valley-Hall edge states *Phys. Rev. Lett.* **120** 063902
- [13] Gao F, Xue H, Yang Z, Lai K, Yu Y, Lin X, Chong Y, Shvets G and Zhang B 2018 Topologically-protected refraction of robust kink states in valley photonic crystals *Nat. Phys.* **14** 140–4
- [14] Wu X, Meng Y, Tian J, Huang Y, Xiang H, Han D and Wen W 2017 Direct observation of valley-polarized topological edge states in designer surface plasmon crystals *Nat. Commun.* **8** 1304
- [15] Qiu P, Liang R, Qiu W, Chen H, Ren J, Lin Z, Wang J X, Kan Q and Pan J Q 2017 Topologically protected edge states in graphene plasmonic crystals *Opt. Express* **25** 22587–94
- [16] Haldane F D and Raghu S 2008 Possible realization of directional optical waveguides in photonic crystals with broken time-reversal symmetry *Phys. Rev. Lett.* **100** 013904
- [17] Raghu S and Haldane F D M 2008 Analogs of quantum-Hall-effect edge states in photonic crystals *Phys. Rev. A* **78** 033834
- [18] Ochiai T and Onoda M 2009 Photonic analog of graphene model and its extension Dirac cone, symmetry, and edge states *Phys. Rev. B* **80** 155103
- [19] Ochiai T 2012 Photonic realization of the (2 + 1)-dimensional parity anomaly *Phys. Rev. B* **86** 075152
- [20] Wang Z, Chong Y D, Joannopoulos J D and Soljacic M 2008 Reflection-free one-way edge modes in a gyromagnetic photonic crystal *Phys. Rev. Lett.* **100** 013905
- [21] Wang Z, Chong Y, Joannopoulos J D and Soljacic M 2009 Observation of unidirectional backscattering-immune topological electromagnetic states *Nature* **461** 772–5
- [22] Lu L, Joannopoulos J D and Soljačić M 2014 Topological photonics *Nat. Photon.* **8** 821–9
- [23] He C, Lin L, Sun X C, Liu X P, Lu M H and Chen Y F 2014 Topological Photonic States *Int. J. Mod. Phys. B* **28** 1441001
- [24] Wu Y, Li C, Hu X, Ao Y, Zhao Y and Gong Q 2017 Applications of topological photonics in integrated photonic devices *Adv. Opt. Mater.* **5** 1700357
- [25] Poo Y, Wu R X, Lin Z, Yang Y and Chan C T 2011 Experimental realization of self-guiding unidirectional electromagnetic edge states *Phys. Rev. Lett.* **106** 093903
- [26] Ao X, Lin Z and Chan C T 2009 One-way edge mode in a magneto-optical honeycomb photonic crystal *Phys. Rev. B* **80** 033105
- [27] Skirlo S A, Lu L, Igarashi Y, Yan Q, Joannopoulos J and Soljacic M 2015 Experimental observation of large Chern numbers in photonic crystals *Phys. Rev. Lett.* **115** 253901
- [28] Yang Y, Poo Y, Wu R, Gu Y and Chen P 2013 Experimental demonstration of one-way slow wave in waveguide involving gyromagnetic photonic crystals *Appl. Phys. Lett.* **102** 231113
- [29] Li Q, Li Z and Wu R 2015 Bending self-collimated one-way light by using gyromagnetic photonic crystals *Appl. Phys. Lett.* **107** 241907
- [30] Fang Y, Ni Z, Xu Q, Zhou J and Wu Y 2016 Transformation of unidirectional modes and split of channel through a cross waveguide *Opt. Commun.* **366** 13–6
- [31] Poo Y, He C, Xiao C, Lu M H, Wu R X and Chen Y F 2016 Manipulating one-way space wave and its refraction by time-reversal and parity symmetry breaking *Sci. Rep.* **6** 29380
- [32] Xiao C, Wu R X, Sa Z H and Zou D Y 2016 Manipulating radiation beams by symmetry of magnetic photonic crystals *Opt. Express* **24** 15042–9
- [33] Xu X, Yao W, Xiao D and Heinz T F 2014 Spin and pseudospins in layered transition metal dichalcogenides *Nat. Phys.* **10** 343–50
- [34] Morozov S V, Novoselov K S, Katsnelson M I, Schedin F, Ponomarenko L A, Jiang D and Geim A K 2006 Strong suppression of weak localization in graphene *Phys. Rev. Lett.* **97** 016801
- [35] Gorbachev R V, Tikhonenko F V, Mayorov A S, Horsell D W and Savchenko A K 2007 Weak localization in bilayer graphene *Phys. Rev. Lett.* **98** 176805
- [36] Pozar D M 1998 *Microwave Engineering* 2nd edn (New York: Wiley) pp 497–517
- [37] Wohlfarth E 1980 *Handbook of Magnetic Materials* vol 2 (New York: Elsevier) p 293
- [38] Xiao D, Liu G B, Feng W, Xu X and Yao W 2012 Coupled spin and valley physics in monolayers of MoS₂ and other group-VI dichalcogenides *Phys. Rev. Lett.* **108** 196802
- [39] Liu S Y, Du J J, Lin Z F, Wu R X and Chui S T 2008 Formation of robust and completely tunable resonant photonic band gaps *Phys. Rev. B* **78** 155101
- [40] Liu S Y, Lu W L, Lin Z F and Chui S T 2010 Magnetically controllable unidirectional electromagnetic waveguiding devices designed with metamaterials *Appl. Phys. Lett.* **97** 201113

- [41] Chen H J, Lu W L, Li J J, Yu J J, Lin Z F, Chan C T and Liu S Y 2017 Manipulating unidirectional edge states via magnetic plasmonic gradient metasurfaces *Plasmonics* **12** 1079–90
- [42] Bi L, Hu J, Jiang P, Kim D H, Dionne G F, Kimerling L C and Ross C A 2011 On-chip optical isolation in monolithically integrated non-reciprocal optical resonators *Nat. Photon.* **5** 758–62
- [43] Bahari B, Ndao A, Vallini F, El Amili A, Fainman Y and Kanté B 2017 Nonreciprocal lasing in topological cavities of arbitrary geometries *Science* **358** 636–40